Ann. Geophys., 25, 1183–1197, 2007
www.ann-geophys.net/25/1183/2007/
© European Geosciences Union 2007

Annales Geophysicae

Solar cycle changes in the geo-effectiveness of small-scale solar wind turbulence measured by Wind and ACE at 1 AU

M. L. Parkinson, R. C. Healey, and P. L. Dyson

Department of Physics, La Trobe University, Victoria 3086, Australia

Received: 1 January 2007 – Revised: 23 March 2007 – Accepted: 7 May 2007 – Published: 4 June 2007

Abstract. Multi-scale structure of the solar wind in the ecliptic at 1 AU undergoes significant evolution with the phase of the solar cycle. Wind spacecraft measurements during 1995 to 1998 and ACE spacecraft measurements during 1997 to 2005 were used to characterise the evolution of small-scale (∼1 min to 2 h) fluctuations in the solar wind speed v_{sw}, magnetic energy density B^2, and solar wind ε parameter, in the context of large-scale (∼1 day to years) variations. The large-scale variation in ε most resembled large-scale variations in B^2. The probability density of large fluctuations in ε and B^2 both had strong minima during 1995, a familiar signature of solar minimum. Generalized Structure Function (GSF) analysis was used to estimate inertial range scaling exponents a_{GSF} and their evolution throughout 1995 to 2005. For the entire data set, the weighted average scaling exponent for small-scale fluctuations in v_{sw} was a_{GSF}=0.284±0.001, a value characteristic of intermittent MHD turbulence (>1/4), whereas the scaling exponents for corresponding fluctuations in B^2 and ε were a_{GSF}=0.395±0.001 and 0.334±0.001, respectively. These values are between the range expected for Gaussian fluctuations (1/2) and Kolmogorov turbulence (1/3). However, the scaling exponent for ε changed from a Gaussian-Kolmogorov value of 0.373±0.005 during 1997 (end of solar minimum) to an MHD turbulence value of 0.247±0.004 during 2003 (recurrent fast streams). Changes in the characteristics of solar wind turbulence may be reproducible from one solar cycle to the next.

Keywords. Magnetospheric physics (Solar wind-magnetosphere interactions) – Space plasma physics (Nonlinear phenomena; Turbulence)

Correspondence to: M. L. Parkinson
(m.parkinson@latrobe.edu.au)

1 Introduction

The Sun's magnetic field reconfigures on 11-year, 22-year, and longer cycles (Carroll and Ostlie, 1996) leading to variations in solar wind turbulence that may be reproducible from one solar cycle to the next, such as those associated with recurrent fast stream flows during the declining phase (Neugebauer and Snyder, 1966; Burlaga, 1995). It is important to characterise the long-term evolution of solar wind turbulence because it affects the coupling of solar wind energy to the magnetosphere, and the initiation of geomagnetic storms. There is also evidence that changes in the solar wind may affect tropospheric climate (e.g. Svensmark and Friis-Christensen, 1997; Reid, 1999; Rycroft et al. 2000).

It is widely accepted that the frequency and intensity of geomagnetic storms is related to the ever changing state of the solar wind impacting the Earth. The aim of this study is to characterise the evolution of small-scale (∼1 min to 2 h) solar-wind turbulence in the context of large-scale behaviour (∼1 day to years) using long-term spacecraft data sets, with a view towards the impact of those variations on the magnetosphere and ionosphere. To achieve this aim, we will analyse Wind (1995 to 1998) and Advanced Composition Explorer (ACE) (1998 to 2005) spacecraft data recorded near the L1 point.

The solar wind ε parameter (Perreault and Akasofu, 1978) provides a measure of the fraction of solar wind Poynting flux entering the magnetosphere via magnetic reconnection:

$$\varepsilon = v_{SW}\frac{B^2}{\mu_0}l_0^2\sin^4\left(\frac{\theta}{2}\right) \tag{1}$$

where v_{sw} is the solar wind speed, B^2 is the magnetic energy density, $l_0^2 = (7\,R_E)^2$ is an effective cross sectional area, and $\theta = \arctan\left(\left|B_y\right|/B_z\right)$ is the clock angle of the interplanetary magnetic field (IMF). The B_y and B_z components are usually expressed in Geocentric Solar Magnetospheric (GSM) co-ordinates.

Published by Copernicus GmbH on behalf of the European Geosciences Union.

In reconnection theory, the IMF clock angle plays a major role in controlling the coupling of solar wind energy to the magnetosphere. The coupling greatly increases when the IMF points in the negative B_z, or southward direction ($\theta=\pi$) because this satisfies the condition for anti-parallel merging. Clearly, fluctuations in v_{sw}, B^2 and θ must combine in complicated ways to produce fluctuations in ε. The evolution of all of these terms will be investigated here using techniques which test for extended self-similarity (Benzi et al., 1993; Bershadskii and Sreenivasan, 2004).

Equation (1) implies that turbulence in the solar wind must affect the rate of magnetic reconnection. Borovsky and Funsten (2003) have also shown that solar wind turbulence plays an important role in the viscous interaction. They showed that enhanced MHD turbulence, as measured by the vector sum of the standard deviations of B_y and B_z, increases the eddy viscosity and thus also the momentum transfer from the solar wind to the magnetosphere. They showed this effect accounts for $\sim$150 nT of the variation in the AE index regardless of whether B_z is southward or northward. The viscous interaction is not captured by Eq. (1).

Early studies of turbulence involved calculating the power spectra of fluctuating measures. In the case of forward energy cascades, three basic scaling regimes were identified in the spectra: a large-scale driving regime, an inertial turbulent regime, and a small-scale dissipation regime. Of course, different systems can exhibit more complicated behaviour including the presence of intermediate scaling regimes, and there are many kinds of turbulence and even more theories to explain them. Identification of scaling exponents helps to constrain the correct physical theory applicable to a complex system.

In basic Kolmogorov hydrodynamic turbulence (Kolmogorov, 1941, 1962) (K41 hereafter), the spectral energy density in the inertial range has a power law decay $f^{-\beta}$ with exponent β=5/3. For MHD/Alfvénic turbulence, as described by Irosnikov (1964) and Kraichnan (1965) (IK hereafter), the spectral exponent is β=3/2. Fluctuations in v_{sw} are anisotropic, exhibiting K41 phenomenology in the field parallel direction, yet IK phenomenology in the field perpendicular direction (Chapman and Hnat, 2007[1]). These authors also found that fluctuations in B^2 exhibit K41 phenomenology. The fluctuations may also be multi-modal in the sense that separate physical processes affect the measures (e.g., the passage of solar wind shocks). All of these complexities affect coupling of energy to the magnetosphere.

Burlaga and Forman (2002) and Burlaga and F.-Viñas (2004a, b) described multi-scale structure in the fluctuations of solar wind speed (v_{sw}) at 1 AU for various phases of the solar cycle. In particular, Burlaga and F.-Viñas (2004b) analysed fluctuations in v_{sw} and B made during 2003 when recurrent corotating fast streams became prevalent, a reproducible feature of the declining phase of solar activity. They found the PDFs of fluctuations in v_{sw} and B from small ($\sim$1 h) to large scales ($\sim$1 year) could be described by a modified form of the Tsallis distribution (Tsallis, 1988). The Tsallis distribution represents an extension of Boltzmann-Gibbs statistical mechanics to include non-equilibrium systems with scaling properties described by fractal and multi-fractal structure. The use of this distribution opens the way toward a comprehensive empirical model of fluctuations in the solar wind, which predictive models must ultimately reproduce.

Fluctuations in v_{sw} are multi-fractal at small to intermediate scales (Burlaga, 1995), exhibiting leptokurtic PDFs at small scales, and becoming Gaussian at intermediate scales (Burlaga and F.-Viñas, 2004a). The convergence toward Gaussian PDFs is consistent with the Central Limit Theorem (e.g. Tijms, 2004), but occurs at smaller τ than for other solar wind parameters. Burlaga and F.-Viñas (2004a) also suggested fluctuations in B were caused by the combination of intermittent turbulence, shocks, discontinuities, and multi-scale filamentary structures.

Horbury et al. (1996) analysed Ulysses measurements of fast solar wind flows emanating from the Sun's southern polar coronal hole. The high-latitude turbulence was described as unevolved, exhibiting strong IK phenomenology close to the Sun, yet with K41 phenomenology at small scales. The minimum cut-off frequency for the K41 range was found to decrease with heliocentric distance. That is, the turbulence became more K41-like at larger scales with increasing heliospheric distance. They used the Ruzmaikin et al. (1995) two component model to correct the scaling exponents for intermittency, and suggested the small-scale fluctuations exhibited an underlying IK phenomenology.

Although statistical, these highly successful studies of solar wind turbulence have been "case studies" in the sense that they have analysed a set of measurements made at a particular heliospheric location and phase of solar activity. There are dangers in scaling properties of solar wind parameters using one or two years of data made at similar locations within the heliosphere. This is because solar wind turbulence is always evolving in space and time, partly driven by constant changes in the dynamics of the solar atmosphere. A more comprehensive picture of solar wind turbulence will be attained when solar wind parameters have been analysed at many heliospheric locations across multiple cycles of solar activity.

Yordanova et al. (2005) found that turbulence in the magnetospheric cusp was anisotropic, exhibiting Gaussian-like behaviour in the field parallel direction (β=2.41), yet more K41-like behaviour in the field perpendicular direction (β=1.93). Crosby et al. (2005) found the power law decay of electron count rate distributions in the outer radiation belts had smaller exponents β during 1995 when there were more fast streams in the solar wind. In this case, the smaller exponents β meant that larger count rates became more frequent

[1]Chapman, S. C. and Hnat, B.: Kolmogorov and Irosnikov-Kraichnan scaling in the anisotropic turbulent solar wind, Phys. Rev. Lett., in review, 2007.

relative to small count rates during 1995. Enhanced solar wind complexity was shown to increase complexity in the energisation of the outer radiation belt.

Freeman et al. (2000) and Uritsky et al. (2001) have investigated the extent to which fluctuations in the magnetosphere are forced by fluctuations in the solar wind, or organised internally, or are a combination of both. A multi-year study of this kind may be a stepping stone to the solution of this outstanding problem. For example, if long-term changes in solar wind scalings are found to be similar to those for indices of magnetospheric activity, then one might conclude the internal fluctuations were directly driven by the solar wind fluctuations. The following analysis will emphasise long-term variability in the solar wind ε parameter and all of its components with a view toward future comparisons with ionospheric and magnetospheric activity.

2 Spacecraft instruments and data sets

This study utilises solar wind parameters measured using the Wind spacecraft during 1995 to 1998 and the ACE spacecraft during 1997 to 2005. This 11-year interval encompassed one solar minimum (1996) to nearly the next (2006). Data from two spacecraft were used to cross-check the validity of our results which are extremely sensitive to any changes in instrumental performance.

The ACE spacecraft was located in a halo orbit at the Earth-Sun L1 point at $\sim$238 R_E. The trajectory of Wind was complicated, including near Earth orbits and excursions to the halo region of ACE. Any Wind measurements that could have been influenced by the magnetosphere were rejected in this study. Statistically, the characteristics of solar wind fluctuations should be the same for two spacecraft which are located in essentially the same region of the heliosphere.

Wind spacecraft instruments included the Solar Wind Experiment (SWE) (Ogilvie et al., 1995) and the Magnetic Field Investigation (MFI) (Lepping et al., 1995). The SWE instrument included 2 Faraday cup ion detectors measuring solar wind protons and alpha particles at energies up to 8 keV. The MFI instrument consisted of dual, wide dynamic range ($\pm$0.001 to $\pm$65 536 nT) triaxial fluxgate magnetometers. The CDAWeb site was used to download SWE measurements of the solar wind speed v_{sw}, and MFI measurements of the IMF magnitude B, and the B_y and B_z components expressed in GSM co-ordinates.

ACE spacecraft instruments include the Solar Wind Electron, Proton, and Alpha Monitor (SWEPAM) (McComas et al., 1998) and the MAGnetometer experiment (MAG) (Smith et al., 1998). The SWEPAM instrument was built using spare (but improved) solar wind electron and ion analysers from the Ulysses mission. Except for minor modifications, the MAG experiment was a flight spare of the Wind mission, and produced data with similar digital resolution and dynamic range. The ACE Level 2 web site was used to download science calibrated data including SWEPAM measurements of v_{sw}, and MAG measurements of B, GSM B_y, and GSM B_z.

Figure 1 is a bar chart showing the number of (a) Wind v_{sw} samples per annum and (b) Wind B samples per annum (both blue). The v_{sw} data were available at a variable time resolution, though τ_0=84 s was close to the average sampling interval. The B data were available at a time resolution of τ_0=92 s. The data were presumably averaged to these sample rates to reduce uncertainty. Figure 1 also shows the number of ACE v_{sw} and B samples per annum (red). The ACE v_{sw} data were available at τ_0=64 s, whereas the B data were available at τ_0=16 s; hence the large number of B samples. Data collection was fairly continuous throughout all years except for B data during 1997, and v_{sw} data commenced on day 36 during 1998.

Ideally, for a long term study of this kind, the detectors on Wind and ACE should have had identical performance characteristics, there should have been no long-term drifts in their performance, and the signal processing algorithms should also have been identical. The mode of operation of the Wind SWE experiment became more complicated during 1998, and this introduced some artificial jumps in the v_{sw} data. For this reason, all data tagged with a quality flag of 4098 or 14 466 were rejected. The Wind B data also had artificial positive spikes B_i which were readily identified and rejected whenever $(B_i - B_{i-1})/B_{i-1} > 0.8$ and $(B_i - B_{i+1})/B_{i+1} > 0.8$ (R. Lepping, private communication, 2006). Rejecting these data resulted in agreement between the 6th order statistical moments of fluctuations in v_{sw} and B^2 measured using Wind and ACE during 1998, the year of common observations. The 6th order moments are extremely sensitive to anomalous values. It is remarkable that the different spacecraft data sets agreed to such a high statistical order after allowing for known problems.

3 Observations and analysis

3.1 Evolution of large-scale solar wind fluctuations

First we provide an overview of large-scale variability in solar and solar wind activity to put the subsequent analysis of small-scale solar wind fluctuations in context. Figure 2a shows the daily 10.7 cm solar flux (red) and sunspot number (blue) during 1995 to 2006. The 27-day running averages have been superimposed (black curve). Hence we emphasis temporal variability at τ=1 day, 27 day, and longer. Solar activity minimised during 1996, including a minimum in the fluctuation level of 10.7 cm solar flux and sunspot number at τ=1 day. Sunspot maximum was during 2000, but continued into 2001 before the declining phase commenced.

Figure 2b shows the daily average v_{sw} and the corresponding 27-day running average at 1 AU calculated using Wind (blue) and ACE (red) measurements. It can be seen that the 27-day average v_{sw} and 1-day fluctuations in v_{sw} minimised

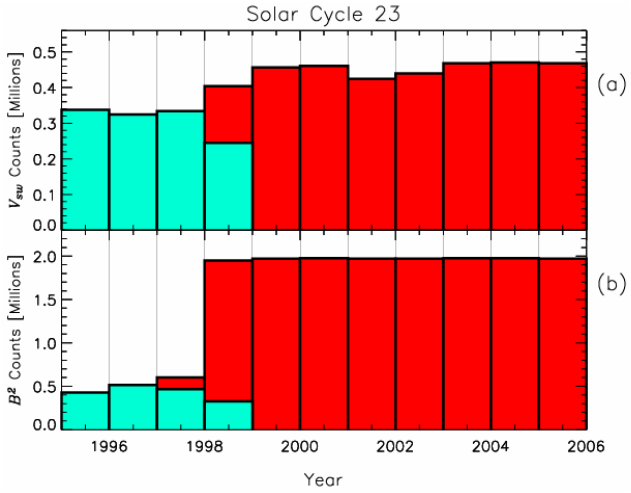

Fig. 1. (a) The number N of solar wind speeds measured at τ_0=84 s using the SWE instrument on the Wind spacecraft during 1995 to 1998 (blue), and at τ_0=64 s using the SWEPAM instrument on the ACE spacecraft during 1998 to 2004 (red). **(b)** The number N of IMF samples measured at τ_0=92 s using the MFI instrument on Wind spacecraft during 1995 to 1998 (blue) and at τ_0=16 s using the MAG instrument on the ACE spacecraft during 1997 to 2005 (red).

during 1997, slightly after sunspot minimum. Another striking feature was the prevalence of recurrent fast streams during the declining phase, with the 27-day average speed peaking during 2003. A significant episode of unusually fast stream was also encountered at the beginning of 2005.

Figure 2c shows the large-scale variability in the magnetic energy density, B^2. It can be seen that B^2 and 1- and 27-day fluctuations in B^2 minimised during 1996, a distinct signature of sunspot minimum. Three episodes of unusually large 1-day average $B^2 > 100\,\mathrm{nT}^2$ occurred during the solar maximum years 2000 and 2001. The largest peak in B^2, for example, was associated with an intense geomagnetic storm starting on 31 March 2001 (K_p=9- and D_{st}=−387 nT). However, the largest 27-day average B^2 of all was coincident with a sharp peak in 27-day average v_{sw} (part b) during 2003. This event was associated with a major geomagnetic storm starting on 29 October (K_p=9 and D_{st}=−383 nT). Another intense storm commenced on 20 November 2003.

Figure 2d shows large-scale variability in the 1- and 27-day average ε parameter. Equation (1) implies the variations in ε are controlled by the variations in v_{sw} and B^2, but the relative variations in B^2 (part c) are much larger than the relative variations in v_{sw} (part b). Thus the variations in ε most resemble the variations in B^2. Like B^2, it can be seen that ε and 1- and 27-day fluctuations in ε minimised during 1996. Moreover, episodes of unusually large $\varepsilon > 2\times10^{10}$ W tended to correspond to the aforementioned episodes of unusually large B^2. The 27-day average ε reached $\sim 5\times10^{10}$ W during the major geomagnetic storms, but peaked at even larger values for shorter intervals.

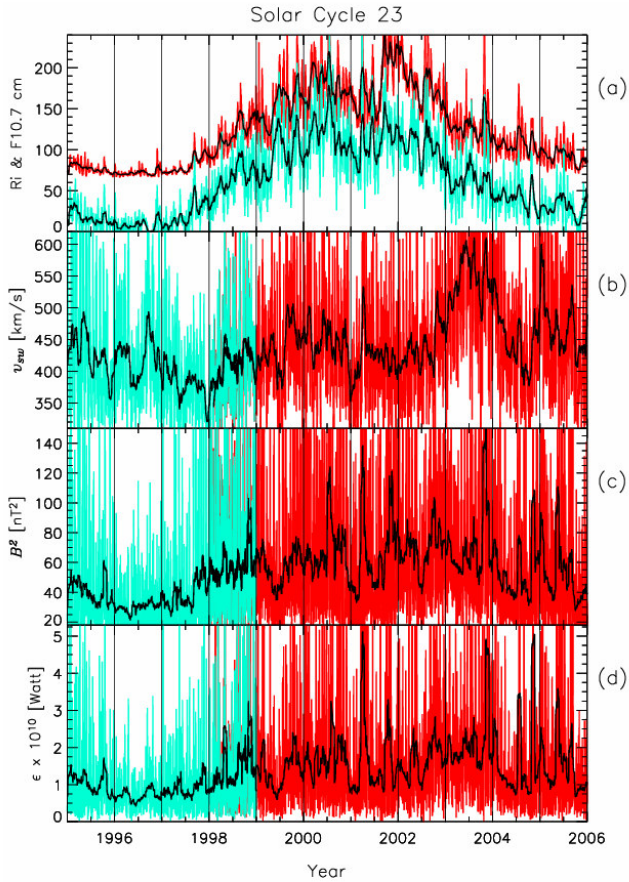

Fig. 2. (a) Daily 10.7 cm solar flux measurements (red) and sunspot numbers (blue) during the study interval 1995 to 2006. **(b)** Daily average solar wind speed v_{sw} measured by Wind (blue) and ACE (red). **(c)** Daily average IMF B^2 measured by Wind (blue) and ACE (red). **(d)** Daily average solar wind ε parameter calculated using Wind (blue) and ACE (red) measurements. The 27-day running averages have been superimposed for all parameters (black curves).

Although useful, the curves in Fig. 2 do not quantify changes in the higher order statistical moments of the solar wind parameters.

3.2 Evolution of small-scale fluctuations in v_{sw}

A fluctuation in the solar wind parameter x was defined as $\delta x(t,\tau)=x(t)-x(t-\tau)$ where τ is an adjustable temporal scale. It is convenient to employ octaves of temporal scale, so that $\tau=2^i\tau_0$ where i is an integer and τ_0 is the native time resolution of the data. The probability density of a fluctuation at scale τ is $n/(N\Delta x)$ where N is the total number of δx samples, and δn is the number of δx samples within bins of size Δx. Hence the probability density function (PDFs) consist of all the elements $P(\delta x,\tau)$ separated according to fluctuation size δx and temporal scale τ.

In this study the fluctuations δx at all scales τ were estimated by stepping through the records at the native resolution

τ_0. This had the advantage of generating numerous δx samples at the largest τ, but it also meant the samples were only completely independent of each other at τ=τ_0, and then gradually became less statistically independent at the largest τ. For example, at τ=524288 s there are only ∼60 completely independent samples, and the corresponding PDFs are less reliable. However, our scaling exponents were not estimated using the under-sampled fluctuations at the largest τ.

Figure 3 summarises the evolution of PDFs of δv_{sw} with solar phase. Wind measurements were used to calculate PDFs of δv_{sw} at τ=84, 168, ..., 688 128 s for each year during 1995 to 1998, and ACE measurements to calculate PDFs of δv_{sw} at τ=64, 128, ..., 524 288 s for each year during 1998 to 2005. Showing the PDFs for all years and τ would be impractical. Hence, Fig. 3a shows the PDFs for Wind at τ=84 s and for ACE at τ_0=64 s, colour coded according to year.

Figure 3a shows that at these short ∼1 min temporal scales, the probability density for large δv_{sw} minimised during 1997 (purple) and then maximised during the fast streams of 2003 (orange). Similar results were obtained when using larger values of τ for Wind or ACE. Figure 2b showed the same basic behaviour extended out to τ∼1 day.

Figures 3b and c summarise the evolution of the PDFs across all τ. Panel (b) shows the evolution of probability density integrated over the peaks of the PDFs using the limits of integration [−2, 2] km s^{-1}. Panel (c) shows the evolution of probability density integrated over the wings of the PDFs using the limits of integration [−500, −20] plus [20, 500] km s^{-1}. The integrated probability densities were calculated separately for each τ, ranging from 84 s (black, bold), to 688 128 s (red) for Wind, and from 64 s (black, bold) to 524 288 s (red) for ACE.

Figure 3b shows that the probability density integrated across the peaks had a maximum value of 0.63 for Wind at τ=84 s during 1997. The probability density integrated across the limits [−∞, ∞] is one, meaning that 100% of δx values are contained within those limits. Hence 63% of fluctuations were contained within [−2, 2] km s^{-1} at τ=84 s. In general, the probability density across the peaks declined with increasing τ; it was only 0.016 at τ=688 128 s during 1997.

A decrease in probability density across the peaks with τ must be compensated by an increase in probability density across the wings with τ, and vice versa. Figure 3c confirms the reduction in probability density across the peaks was compensated by an increase of probability density across the wings. During 1997, the integrated probability density across the wings was only 4.8×10^{-4} at τ=92 s, increasing to 0.64 at τ=688 128 s. As expected, larger fluctuations in v_{sw} tended to occur at larger temporal scales.

Figures 3b and c show the evolution of probability density with solar phase throughout 1995 to 2005. Most of the trends shown in this and subsequent figures are considered statistically significant because they are consistent across a broad range of τ and the PDFs were calculated using many thousands of independent samples, especially at low to moderate τ (Fig. 1). However, some of the erratic variations shown at the largest τ may have been statistically insignificant because of the decreasing number of independent samples.

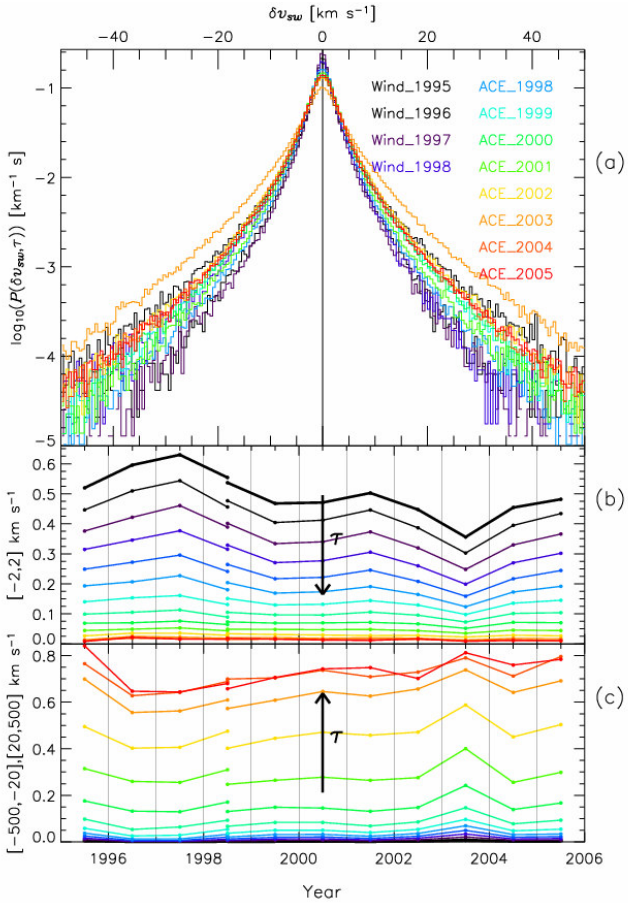

Fig. 3. (a) The evolution of annual PDFs for solar wind speed fluctuation δv_{sw} calculated for Wind at τ_0=84 s and for ACE at τ_0=64 s. The PDFs were colour coded according to year. **(b)** The evolution of probability density integrated over the peaks of the PDFs using the limits of integration [−2, 2] km s^{-1}. **(c)** The evolution of probability density integrated over the wings of the PDFs using the limits of integration [−500, −20] plus [20, 500] km s^{-1}. The results for (b) and (c) were calculated separately at each τ, ranging from 84 s (black) to 688 128 s (red) for Wind, and from 64 s (black) to 524 288 s (red) for ACE.

Figure 3b shows that for all τ the probability density integrated across the peaks maximised during 1997, just past sunspot minimum, and then declined toward a minimum during the fast streams of 2003. For example, at τ ∼1 min, the absolute solar cycle change in probability density integrated across the peaks was >27% (i.e. using τ=84 s for 1997 and τ=64 s for 2003). Conversely, Figure 3c shows the probability density integrated across the wings minimised during 1997, and then increased toward a maximum during 2003.

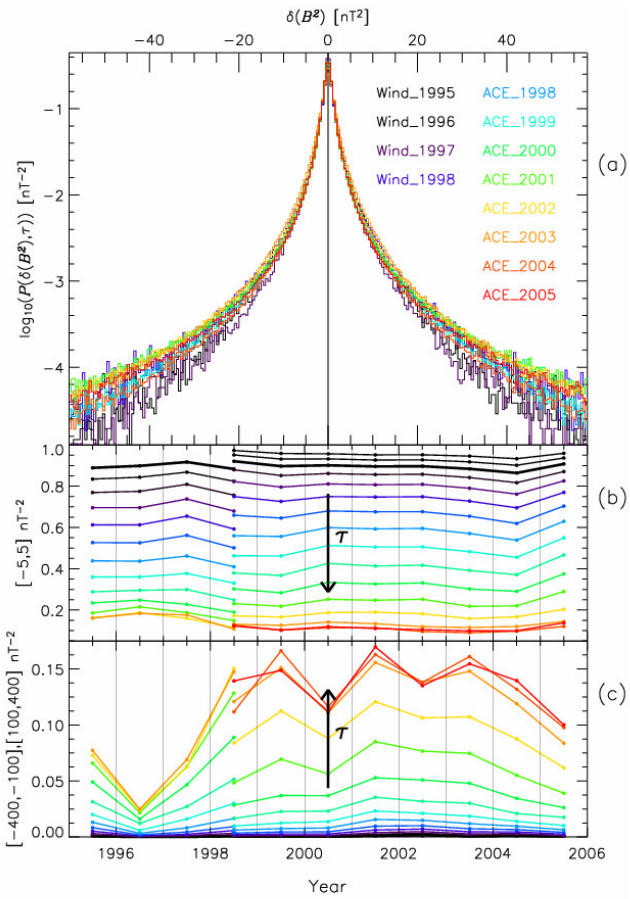

Fig. 4. (a) The evolution of annual PDFs for magnetic energy density fluctuation $\delta(B^2)$ calculated for Wind at τ_0=92 s and for ACE at τ_0=64 s. The PDFs were colour coded according to year. **(b)** The evolution of probability density integrated over the peaks of the PDFs using the limits of integration $[-5, 5]\,\mathrm{nT}^2$. **(c)** The evolution of probability density integrated over the wings of the PDFs using the limits of integration $[-400, -100]$ plus $[100, 400]\,\mathrm{nT}^2$. The results for (b) and (c) were calculated separately for at each τ, ranging from 92 s (black) to 376 832 s (red) for Wind, and from 16 s (black) to 524 288 s (red) for ACE.

For example, at $\tau\sim$1 day, the change in integrated probability density across the wings was >18% (i.e. using τ=86 016 s for 1997 and τ=65 536 s for 2003; yellow curves).

Furthermore, in going from 1997 to 2003, the absolute decrease in probability density across the peaks was greatest for $\tau\sim$1 min, and the corresponding increase in probability density across the wings was greatest for $\tau>1$ day. Whilst the probability density was transferred from small δv_{sw} to large δv_{sw} at all τ, the probability density was also transferred from short τ to long τ. The transfer of probability density was toward greater τ as well as greater δv_{sw}.

The ordinates in Figs. 3b and c were enlarged to reveal the variations in near zero probability density. The relative variations in probability density were comparable at all τ. Plotting the results on a logarithmic scale did not help because this rendered the largest variations in probability density invisible.

3.3 Evolution of small-scale fluctuations in B^2

Figure 4 summarises the evolution of the PDFs of fluctuations in magnetic energy density B^2 with solar phase, in the same format as Fig. 3. Wind measurements were used to calculate PDFs of $\delta(B^2)$ at τ=92, 184, ..., 376 832 s for each of the years 1995 to 1998, and ACE measurements to calculate PDFs of $\delta(B^2)$ at τ=16, 32, ..., 524 288 s for each of the years 1998 to 2005. Figure 4a shows the PDFs for Wind at τ=84 s and for ACE at τ=64 s, colour coded according to year.

Figure 4a shows the solar cycle changes in the PDFs of $\delta(B^2)$ at temporal scales of $\sim$1 min were not as large as those for δv_{sw} (Fig. 3a). The probability density for large $\delta(B^2)$ was smallest during 1996 and 1997 (black, purple), and larger though variable in the remaining years encompassing the solar maximum and declining phase. This is consistent with Fig. 2c which showed that fluctuations in B^2 at τ $\sim$1 day minimised during 1996, and then subsequently increased.

Figure 4b shows the evolution of probability density integrated over the peaks of the PDFs using the limits of integration $[-5, 5]\,\mathrm{nT}^2$. Again the results were calculated separately for each τ. The solar cycle changes in probability density integrated over the peaks were relatively weak at short τ (black), but slightly larger at the largest τ (red). These relatively "flat" changes are consistent with the relatively weak changes in the peaks of the PDFs shown in Fig. 4a.

Figure 4c shows the evolution of probability density integrated over the wings of the PDFs using the limits of integration $[-400, -100]$ plus $[100, 400]\,\mathrm{nT}^2$. Changes in the probability density of very large $\delta(B^2)$ were dramatic: the probability density minimised during 1996 at all τ, and then increased rapidly during 1997 to 1999. For short τ, the integrated probability density only peaked during 2001, whereas for $\tau>1$ day there were local maxima during 1999, 2001, and 2003. Note that the evolution of probability density had greater statistical significance at shorter τ because of the larger number of independent samples. That is, the three local maxima for $\tau>1$ day have less statistical significance than the single maximum at shorter τ.

3.4 Evolution of small-scale fluctuations in ε

Figure 5 summarises the evolution of the PDFs of fluctuations in the solar wind ε parameter with solar phase, in the same format as Fig. 3. Wind measurements were used to calculate PDFs of $\delta\varepsilon$ at τ=84, 168, ..., 688 128 s for each of the years 1995 to 1998, and ACE measurements to calculate PDFs of ε at τ=64, 128, ..., 524 288 s for each of the years 1998 to 2005. As in Fig. 3, panel (a) shows the PDFs for

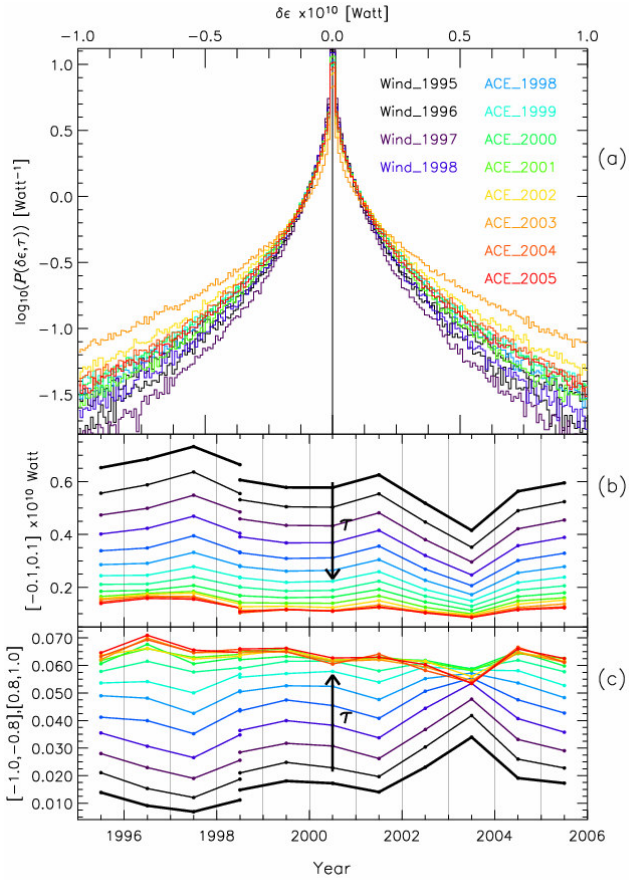

Fig. 5. **(a)** The evolution of annual PDFs for ε parameter fluctuations $\delta\varepsilon$ calculated for Wind at τ_0=92 s and for ACE at τ_0=64 s. The PDFs were colour coded according to year. **(b)** The evolution of probability density integrated over the peaks of the PDFs using the limits of integration $[-0.1, 0.1]\times10^{10}$ Watt. **(c)** The evolution of probability density integrated over the wings of the PDFs using the limits of integration $[-1.0, -0.8]$ plus $[0.8, 1.0]\times10^{10}$ W. The results for (b) and (c) were calculated separately at each τ, ranging from 84 s (black) to 688 128 s (red) for Wind, and from 64 s (black) to 524 288 s (red) for ACE.

Wind at τ=84 s and for ACE at τ_0=64 s, colour coded according to year.

The results shown in Fig. 5 are reminiscent of the results shown in Fig. 3 for δv_{sw}. For example, Fig. 5a shows that at temporal scales of ∼1 min, the probability density for large $\delta\varepsilon$ minimised during 1997, and then maximised during the fast streams of 2003. Figure 3a showed the same for δv_{sw}. However, the PDFs of $\delta\varepsilon$ are more strongly leptokurtic than the PDFs of δv_{sw}, and, unlike the PDFs of δv_{sw}, they do not show a significant transition toward a more Gaussian shape at larger temporal scales (see Fig. 6).

Figure 5b shows the evolution of probability density integrated over the peaks of the PDFs using the limits of integration $[-0.1, 0.1]\times10^{10}$ W. Again the results were calculated separately for each τ. Like the results for δv_{sw}, the

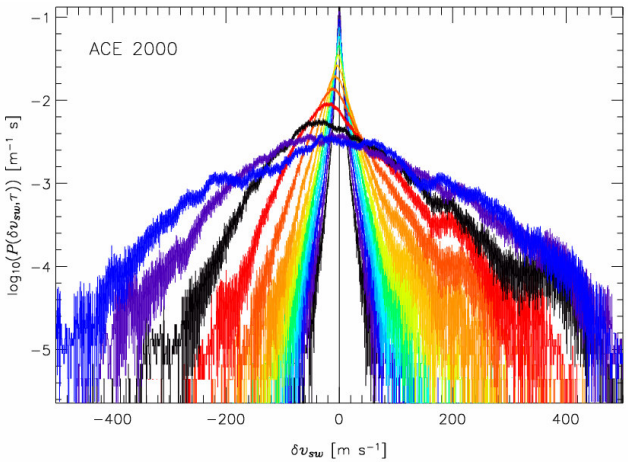

Fig. 6. Probability density functions (PDFs) of the fluctuations in the solar wind speed v_{sw} for year 2000. The different curves correspond to temporal scales τ =64 s (black), 128 s, 256 s, . . . , 524 288 s (6.1 days) (red). Error bars were calculated assuming Gaussian fluctuations $\propto\sqrt{n}/n$, and they have been drawn at the 3σ level. A bin size of 1 km s^{-1} was used.

probability density integrated over the peaks decreased with larger τ for each year. The solar cycle changes in probability density integrated over the peaks were also reminiscent of those for δv_{sw}; the probability denisty maximised during 1997, and then gradually decreased to a minimum during the fast streams of 2003.

Figure 5c shows the evolution of probability density integrated over the wings of the PDFs using the limits of integration $[-1.0, -0.8]$ plus $[0.8, 1.0]\times10^{10}$ W. Like the results for δv_{sw}, the probability density integrated over the wings tended to increase with τ during any one year. The probability density also minimised during 1997, and then gradually increased to a maximum during the fast streams of 2003. However, these trends did not hold for the largest $\tau>1$ day, especially during 2003. Surprisingly, the probability density of large fluctuations at $\tau>1$ day in $\delta\varepsilon$ minimised during 2003.

Hence, unlike δv_{sw}, the transfer of probability density from small to large $\delta\varepsilon$ was strongest for the small-scale fluctuations, ∼1 min to <2 h. That is, there was no transfer of probability density toward greater τ as well as greater $\delta\varepsilon$. Nevertheless, probability density was conserved, and the similarity of the results for δv_{sw} and $\delta\varepsilon$ suggests that solar cycle change in δv_{sw} exerted a stronger influence on solar cycle changes in $\delta\varepsilon$ than $\delta(B^2)$ at small scales <2 h.

3.5 Evolution of small-scale fluctuations in $\sin^4(\theta/2)$

The PDFs of $\delta\sin^4(\theta/2)$ were plotted in the same format as Figs. 3 to 5, but are not shown for brevity. At temporal scales <1 day the probability density integrated across the peaks decreased with increasing τ, whereas the probability density

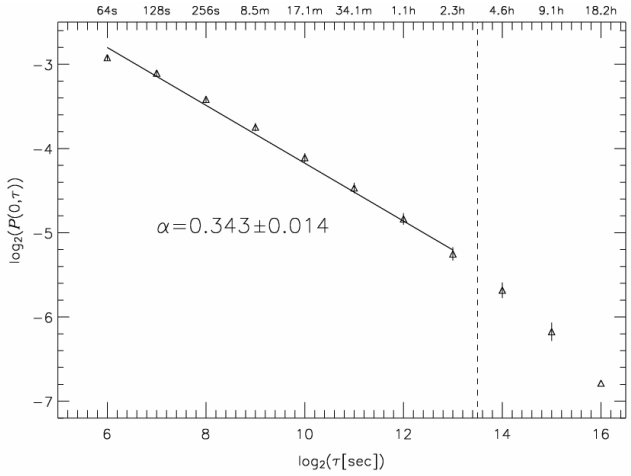

Fig. 7. Scaling of the PDF peaks, $\log_2 P(0,\tau)$ versus $\log_2\tau$, for the δv_{sw} curves shown in Fig. 6. The linear best fit to the data yields a slope of α_0=0.343±0.014 using a PDF bin size of 1 km s^{-1}. The error bars assume Gaussian noise in the peaks, and are drawn at the 3σ level. The vertical dashed line indicates the nominal outer temporal scale for the power law regime.

integrated over the wings tended to increase with increasing τ.

The solar cycle changes in the probability density integrated across the peaks had primary maxima during 1996 (solar minimum) and 2004 (late declining phase). There was also a secondary maximum during 2000 (solar maximum). Conversely, the probability density integrated over the wings had primary maxima in 1996 and 2004, and a secondary maximum during 2000, at most temporal scales <1 day.

However, the solar cycle changes in the PDFs of $\delta\sin^4(\theta/2)$ were not as strong as those found for δv_{sw}, $\delta(B^2)$, and $\delta\varepsilon$, nor did they resemble any of those changes. Given a roughly stationary distribution of IMF clock angles and fluctuations therein, strong solar cycle changes in the PDFs of $\delta\sin^4(\theta/2)$ would not be expected because the sine function is raised to the fourth power.

Figures 3a to 5a show that the leptokurtic behaviour of the PDFs decreased in the following order: $\delta\varepsilon$, $\delta(B^2)$, and δv_{sw}. Nevertheless, the PDFs of δv_{sw} were still strongly leptokurtic, especially at small scales. Although not shown, the PDFs of $\delta\sin^4(\theta/2)$ were the most leptokurtic of all, again because the sine function is raised to the fourth power.

4 Characterisation of small-scale turbulence

4.1 Generalized Structure Function (GSF) analysis

Although power spectra are useful for analysing turbulence, they are calculated using variances, and thus cannot discriminate between Gaussian and non-Gaussian fluctuations (Mandelbrot, 2002). Sornette (2000) describe other analyses which extend our ability to characterise turbulence. Here we make use of peak scaling and Generalised Structure Function (GSF) analyses to help characterise the long-term evolution of small-scale solar wind turbulence. These methods test for extended self-similarity (Benzi et al., 1993; Bershadskii and Sreenivasan, 2004), providing a way to identify mono-fractal regimes and their scaling exponents.

This study focuses on characterising regimes of inertial range turbulence reasonably well described by a single exponent power law over a fixed range of τ. Although these regimes are approximately mono-fractal, they are actually weakly multi-fractal to a greater or lesser extent, depending on the particular parameter and chosen range of τ. When analysed across a sufficiently large range of τ, all the parameters exhibit multi-fractal behaviour, and multi-fractal spectra should be calculated. Departure from linearity in a GSF analysis may indicate either multi-fractal behaviour, or simply poor statistics.

The application of peak scaling and GSF analyses to solar wind and other data have been described by Hnat et al. (2002a, b, 2003, 2005), Chapman et al. (2005), and Parkinson (2006). The limitations of these techniques in the presence of measurement noise and multi-fractal behaviour will be illustrated by an analysis of the fluctuations in v_{sw} for year 2000. Strictly, the fluctuations in v_{sw} are multi-fractal across medium to large scales (Burlaga, 1995). This problem was partly circumvented by identifying a power law scaling exponent using a smaller range of temporal scales than usual, and for which linearity in the GSFs was satisfactory.

Figure 6 shows the PDFs of δv_{sw}, namely $\log_{10}(P(\delta v_{sw},\tau))$ versus δv_{sw}, calculated separately for τ_0 =64 s (black) to τ=524 288 s (6.1 day) (red) for year 2000. The PDFs were strongly leptokurtic at the shortest scales, τ_0=64 s, but became Gaussian and asymmetric at larger scales, τ>8192 s (∼2 h). The asymmetries are related to fast streams overtaking slow flows in the solar wind at 1 AU (Sarabhai, 1963). The transformation to Gaussian PDFs was not prevalent in the PDFs of $\delta(B^2)$, $\delta\sin^4(\theta/2)$, and $\delta\varepsilon$ across the same range of temporal scales.

Peak scaling involves plotting $\log_2(P(0,\tau))$ versus $\log_2\tau$ where $P(0,\tau)$ is the peak amplitude of the PDF at different temporal scale τ. If the peaks follow a power law then $P(0,\tau)\propto\tau^{-\alpha_0}$, and a straight line will be obtained over the applicable range of temporal scale. Hence the gradient gives the peak scaling exponent α_0. Although peak scaling should be accurate because the probability density of returns corresponds to the largest number of samples, the estimation of returns is also the most sensitive to measurement errors, sometimes assumed to be Gaussian. Hence the bin size also affects the estimation of α_0 (Parkinson et al., 2006).

Figure 7 shows $\log_2(P(0,\tau))$ versus $\log_2\tau$ for the PDFs of δv_{sw}. Similar results were obtained for other years. The error bars have been drawn at the 3σ level and the straight line represents the results of a weighted linear regression. The line does not overlap all of the error bars, but a quasi-linear

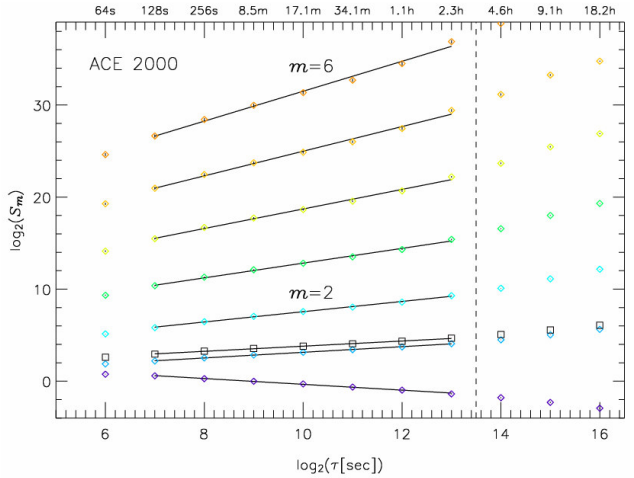

Fig. 8. A generalised structure function (GSF) analysis showing the variation of the moments $S_m(\tau)=\langle|\delta v_{sw}(t,\tau)|^m\rangle$ with temporal scale τ for orders $m=-1$ to 6, but not the trivial results for m=0. The results are quasi-linear on a log-log plot between τ=128 s and ∼2 h. We also show the variation of the standard deviation $\sigma(\tau)=[S_2(\tau)]^{1/2}$ with τ (squares). The error bars are drawn at the 3σ level, and weighted least squares fits have been applied to all the moments.

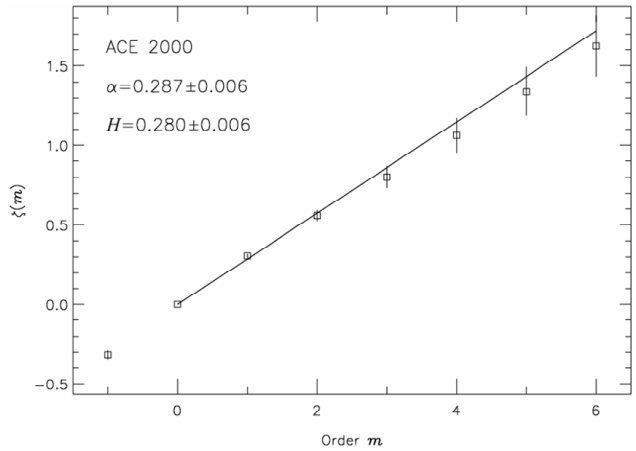

Fig. 9. The gradients of the weighted least squares curves $\zeta(m)$ estimated from Fig. 8, versus order m over the range $m=-1$ to 7. The error bars are drawn at the 3σ level. The gradient of the weighted least squares curve to the $\zeta(m)$ points gives $\alpha_{\rm GSF}$=0.287±0.006 (1σ error).

regime can be identified across ∼2 decades from τ_0=64 s and 8192 s (∼2 h). The restricted scaling regime for δv_{sw} is consistent with its strong multi-fractal behaviour. The scaling exponent obtained for δv_{sw} was K41-like, namely α_0=0.343±0.014 (1σ error). In contrast, the results for $\delta\varepsilon$ exhibit strong linearity from τ=64 s to τ ∼4.5 h (e.g. Hnat et al., 2002b), and possibly τ∼10 h (∼3 decades) (Parkinson et al., 2006).

GSF analysis utilises higher order statistical moments, and thus provides a more comprehensive characterisation of the fluctuations. The GSFs of the fluctuations $\delta x(t,\tau)=x(t)-x(t-\tau)$ are defined as the time average of their moments, $S_m(\tau)=\langle|\delta x(t,\tau)|^m\rangle$ where m is any real number, not necessarily positive. For single exponent scaling of $\delta x(t,\tau)$, $S_m(\tau)\propto\tau^{\zeta(m)}$, and a log-log plot of S_m versus τ will reveal a straight line for each m with gradients $\zeta(m)$. If the time series of x is mono-fractal, then $\zeta(m)=\alpha_{\rm GSF}m$ with a single scaling exponent $\alpha_{\rm GSF}$. A plot of $\zeta(m)$ versus order m is known as a "ζ plot". The parameter $\alpha_{\rm GSF}$ obtained in this way should collapse the PDFs at separate τ onto a single curve.

Figure 8 shows the GSF analysis for δv_{sw} for the year 2000. The moments $S_m(\tau)$ were calculated for $m=-1$ to 6 across a broad range of τ. Like the peak scaling analysis, there is a quasi-linear small-scale regime between τ=128 s and 8192 s (∼2 h). The points at τ_0=64 s have been excluded from the least squares fit because of a slight "roll-off" at these smallest scales. There is clearly a transition in the gradients of all the curves beyond the outer scale of ∼2 h.

Chapman et al. (2005) and Kiyani et al. (2006) discuss methods used to "condition" the data, thereby eliminating the deleterious effects of extreme fluctuations which are invariably under-sampled. The method used to condition the data may affect the estimation of the scaling exponents. In this study, we conditioned the data by rejecting all the δv_{sw} samples greater than 10σ, where σ was estimated independently at all τ. Kiyani et al. (2006) showed the scaling exponents stabilized after removing only a tiny fraction of the samples (<1%).

Figure 8 also shows the variation of the standard deviation $\sigma(\tau)=[S_2(\tau)]^{1/2}$ with τ (squares). The gradient of this curve provides an estimate of the Hurst exponent H. Although useful, H does not discriminate between Gaussian and non-Gaussian distributions (Mandelbrot, 2002).

Figure 9 shows the ζ plot where each $\zeta(m)$ is the gradient of the m-th best fit curves shown in Fig. 8. The weighted least squares fit to the ζ plot was to the points for m=0 to 6, with $\zeta(0)$=0 by definition. The solution was constrained to pass through the origin to ensure mathematical plausibility, and to force a better fit to the lower order moments which are more statistically significant. Multi-fractal behaviour is indicated if $\zeta(m)$ is quadratic in m (Chapman et al., 2005). Hence departure from linearity in the ζ plots, especially for the low order moments, may indicate the presence of multi-fractal behaviour.

Figure 9 shows the increase in the gradients of the best fit curves in Fig. 8 was essentially linear. Hence $\zeta(m)=\alpha_{\rm GSF}m$ with $\alpha_{\rm GSF}$=0.287±0.006 (1σ error), as expected for intermittent IK turbulence. Note that for random fluctuations, $\alpha_{\rm GSF}$=1/2 and $\zeta(2)$=1, for Kolmogorov turbulence, $\alpha_{\rm GSF}$=1/3 and $\zeta(3)$=1, and for IK turbulence, $\alpha_{\rm GSF}$=1/4 and $\zeta(4)$=1 (Table 1).

Table 1. Scaling exponents for single-mode mono-fractal fluctuating measures.

Fluctuation Model	(1) Power spectra	(1) GSF analysis	(2) Linear ζ plot	(3) Fractal dimension
Zero Complexity	β=3	α=1	ζ (1)=1	D =1.0
Gaussian Motion	β=2	α=1/2	ζ (2)=1	D =1.5
Kolmogorov Hydrodynamic	β=5/3	α=1/3	ζ (3)=1	D =1.66
Irosnikov-Kraichnan MHD	β=3/2	α=1/4	ζ (4)=1	D =1.75
Maximum Complexity	β=1	α=0	ζ (∞)=1	D =2.0

(1) β=2α+1
(2) m=α^{-1}
(3) D=2-α

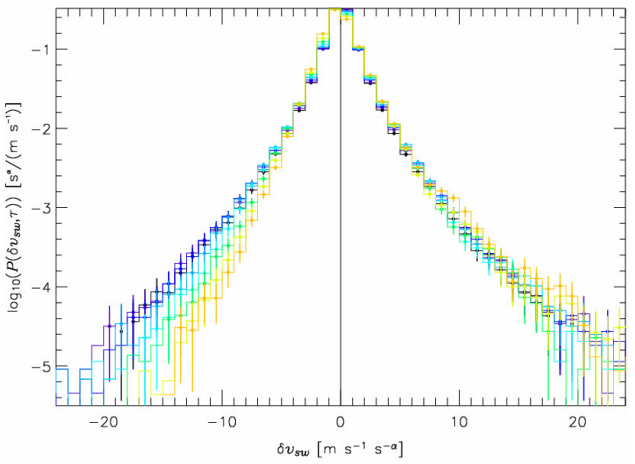

Fig. 10. Partial scaling collapse of the PDFs of δv_{sw} for τ=64 s to 8192 s (∼2 h) shown in Fig. 6 onto a common curve (see text). The scaling exponent $\alpha_{\rm GSF}$=0.287 estimated from Fig. 9 was used in the mapping. Again, the error bars assume Gaussian fluctuations and are drawn at the 3σ level.

Identification of a mono-fractal scaling regime can be validated by using the scaling exponent $\alpha_{\rm GSF}$ to re-scale or "collapse" the PDFs at separate τ onto a single curve using the transformations $P_s(\delta x_s,\tau)$=$\tau^{\alpha_0}P(\delta x,\tau)$ and δx_s=$\delta x\tau^{-\alpha_0}$ where δx=δv_{sw} in this case. Figure 10 shows the extent to which scaling collapse was achieved for PDFs of δv_{sw} from τ_0=64 s (black) to τ =8192 s (∼2 h) (red). The scaling collapse was partly successful except for the asymmetry and multi-fractal behaviour which developed at larger τ. In the case of $\delta\varepsilon$, the scaling collapse is excellent, and holds over another decade of temporal scale (Hnat et al., 2002b, 2003).

4.2 Relationship between complexity and scaling exponents

Table 1 shows the relationship between scaling exponents obtained using power spectra and GSF analysis, and the "complexity" (fractal dimension) of the data. Power spectra separate spectral energy density according to frequency, and can be used to identify power law scaling exponents β, whereas GSF analysis separates probability density according to scale size, and can be used to identify power law exponents α. The two kinds of scaling exponents are related via β=2α+1.

If Gaussian fluctuations control the diffusion of the probability density with τ, then α=1/2 and β=2. If ideal K41 turbulence prevails, then $\alpha_{\rm GSF}$=1/3 and β=5/3, whereas for IK turbulence, α=1/4 and β=3/2. Intermittency in IK turbulence will increase the magnitude of the observed scaling exponents (Ruzmaikin et al., 1995).

Peak scaling separates the peak probability density according to scale size (Fig. 7), in this case temporal. In magnitude, a relatively small scaling exponents $\alpha_0 \ll 1$ implies the variance of fluctuations only decreases slightly at larger scales τ. In other words, as $\alpha_0 \rightarrow 0$ the magnitude of fluctuations becomes equal at all scales. This suggests the time series becomes intensely fractal. In fact, the complexity would be unlimited in τ, except in practise the cascade is usually broken by dissipation at some inner τ, and the physical dimensions of the system driver at some outer τ.

GSF analysis is a more comprehensive way of characterising the fluctuations because it separates the higher order statistical moments according to scale size (Fig. 8). In practise, the maximum useable order is constrained by the sample size N. Relatively small scaling exponents $\alpha_{\rm GSF} \ll 1$ imply the rate of increase of the statistical moments with τ is similar at all orders m. Because $\zeta(0)$=0, this implies that as $\alpha_{\rm GSF} \rightarrow 0$, $\zeta(m) \rightarrow 0$ for all m, and the PDFs of fluctuations become the same for all τ. Again, the time series becomes intensely fractal. Basically, smaller scaling exponents correspond to greater complexity in the sense of increasing fractal dimension.

The fractal dimension D of a time series can be thought of as D=2−α where α=1 implies no complexity and α=0 implies maximum complexity. Thus K41 turbulence (α=1/3) is more complex than Gaussian fluctuations (α=1/2), and IK turbulence (α=1/4) is more complex than K41 turbulence.

4.3 Solar cycle changes in the scaling exponents

The techniques outlined in Sect. 4.1 were used to estimate the scaling exponents α_0, α_{GSF}, and H for each year of the study interval for the three solar wind parameters, v_{sw}, B^2, and ε. Note the behaviour of $\delta\sin^4(\theta/2)$ is intensely non-linear and the use of GSF analysis to estimate a single scaling exponent is impractical.

Figure 11a shows the daily solar activity during 1995 to 2006, reproduced for reference. Figures 11b–d show the evolution of the peak scaling exponent α_0 (blue), GSF scaling exponent α_{GSF} (black), and the Hurst exponent H (red) for the three solar wind parameters. The scaling exponents were calculated separately for each year during 1995 to 2005. Sorting the data according to year kept N large and roughly constant (Fig. 1), as required to maintain statistical significance. The scaling exponents were plotted increasing downward, so that complexity increases upward. The horizontal dashed line represents the scaling exponent expected for K41 turbulence, and the dash-dotted line represents the scaling exponent expected for IK turbulence.

Figure 11b shows the evolution of the scaling exponents estimated for fluctuations in v_{sw} during 1995 to 2005. The peak scaling exponents α_0 were estimated using Wind data from τ=84 to 5376 s and ACE data from τ=64 to 8192 s (∼2 h), whereas GSF scaling exponents α_{GSF} were estimated using Wind data from τ=84 to 5376 s and ACE data from τ=64 to 4096 s. Similar results were obtained when changing the outer temporal scale by one or two octaves. However, for consistency, these ranges of temporal scale were kept constant for all years. Note the error bars have been drawn at the 3σ level.

The measurements recorded by ACE and Wind during 1998 were essentially concurrent and within the same region of the heliosphere. Thus we would expect the estimated scaling exponents to be very similar. For δv_{sw}, the 1σ error bars estimated using Wind and ACE data nearly overlapped during 1998 (α_{GSF}=0.317±0.008 for Wind and α_{GSF}=0.301±0.007 for ACE). The small differences may be explained by the different sampling times and spacecraft locations. However, a GSF analysis involves the calculation of higher order statistical moments which are very sensitive to artefacts. We liaised with the relevant instrument PIs to ensure no suspect data were used in the calculations.

For δv_{sw}, the weighted average peak scaling exponent α_0 for all years was α_0=0.355±0.005 (1σ error). However, the values for Wind were larger than for ACE. Peak scalings are problematic because their estimation is influenced by measurement errors, sometimes assumed to be Gaussian (α=1/2). The Wind α_0 values were probably more strongly influenced by measurement errors than the ACE α_0 values, and both probably over-estimated the true underlying exponents. Peak scaling exponents may provide information about changes in detector performance.

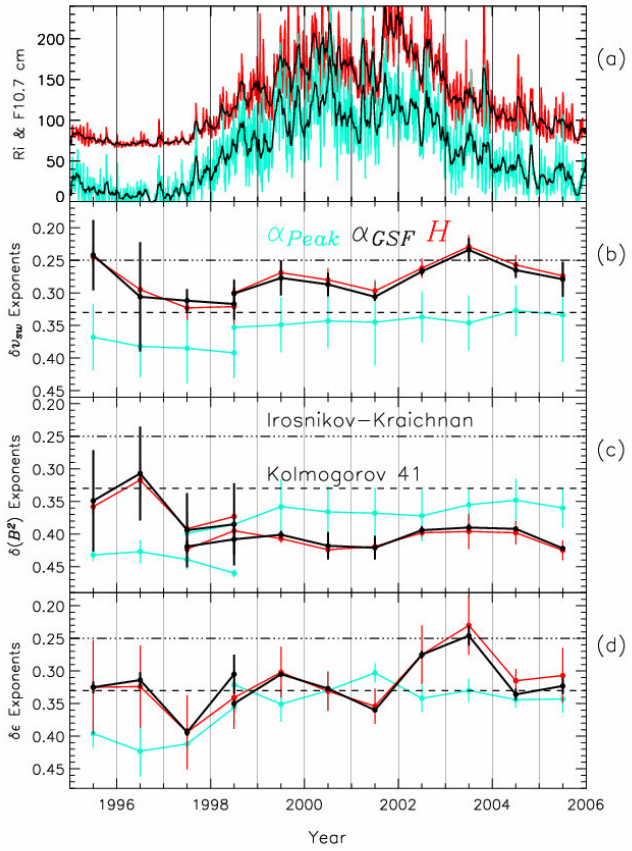

Fig. 11. **(a)** Daily 10.7 cm solar flux measurements (red) and sunspot numbers (blue) during the study interval 1995 to 2006. **(b)** The evolution of annual scaling exponents for fluctuations in solar wind speed δv_{sw}. α_0 was estimated using Wind data from τ=84 to 21 504 s and ACE data from τ=64 to 32 768 s (∼6 h). α_{GSF} and H were estimated using Wind data from τ=84 to 5376 s and ACE data from τ=128 to 8192 s. **(c)** The same as (b) except for fluctuations in magnetic energy density $\delta(B^2)$. α_0 was estimated using Wind data from τ=92 to 47 104 s and ACE data from τ=32 to 37 768 s (∼10 h). α_{GSF} and H were estimated using Wind data from τ=92 to 23 552 s and ACE data from τ=32 to 16 384 s (∼5 h). **(d)** The same as (b) except for fluctuations in the ε parameter. α_0 was estimated using Wind data from τ=84 to 43 008 s and ACE data from τ=64 to 32 768 s (∼9 h). α_{GSF} and H were estimated using Wind data from τ=84 to 5376 s and ACE data from τ=64 to 8192 s (∼2 h).

The GSF scaling exponents are considered more reliable because they were estimated using statistical moments of order m=0 to 6. The use of weighted least squares fits helped to compensate for the reduced statistical significance of the higher order moments. However, the largest error bars drawn in Fig. 11 indicate the ζ plots were less linear, either due to stronger multi-fractal behaviour or the reduced statistical significance of the higher order moments, or both. Also, we may not have eliminated all of the artefacts in the data.

Figure 11b shows the evolution of the scaling exponents α_{GSF} and H estimated for fluctuations in v_{sw}. The weighted

average values for all years were α_{GSF}=0.284±0.001 and H=0.283±0.002. However, the α_{GSF} values ranged between a K41-IK value of 0.317±0.008 during the ascending phase, 1998, to a "beyond IK" value of 0.234±0.006 during the recurrent fast streams of 2003. The relatively large error bars for α_{GSF} estimated during 1995, 1996, and 2005 suggest stronger multi-fractal behaviour near solar minimum, but there may have been subtle variations in the data quality.

Figure 11c shows the evolution of the scaling exponents estimated for fluctuations in B^2 during 1995 to 2005. The parameters α_0 were estimated using Wind data from τ=92 to 11 776 s and ACE data from τ=16 to 8192 s (∼2 h), whereas GSF scaling exponents α_{GSF} were estimated using Wind data from τ=92 to 23 552 s and ACE data from τ=32 to 16 384 s (∼4 h). Linearity was maintained across a larger range of temporal scales than for δv_{sw}. Again, the range of temporal scales was kept constant for all years, and the quality of the scaling collapse varied from one year to the next.

For $\delta(B^2)$, the weighted average scaling exponents for all years were α_0=0.439±0.001, α_{GSF}=0.395±0.001, and H=0.407±0.001. Basically, these values ranged between the values expected for pure Gaussian and K41 fluctuations. Again, the small differences between the Wind and ACE scaling exponents for the years 1997 and 1998 may be explained by the different sampling times and spacecraft locations, and subtle variations in data quality. Both α_{GSF} and H had local minima during 1996, but the error bars were relatively large. The weak local minima in α_{GSF} and H during the recurrent fast streams of 2003 are considered more reliable because of the smaller error bars and consistent data set.

Figure 11d shows the evolution of the scaling exponents estimated for solar wind ε fluctuations during 1995 to 2005. The parameters α_0 were estimated using Wind data from τ=84 to 43 008 s and ACE data from τ=64 to 32 768 s (∼9 h), whereas GSF scaling exponents α_{GSF} were estimated using Wind data from τ=84 to 5376 s and ACE data from τ=64 to 8192 s (∼2 h). As with previous studies (Hnat et al., 2002b, 2003; Parkinson, 2006), scaling collapse was generally excellent for the ε parameter over the chosen range of temporal scale.

For $\delta\varepsilon$, the weighted average scaling exponents for all years were α_0=0.352±0.001, α_{GSF}=0.331±0.001, and H=0.323±0.003. These values are close to the values expected for K41 turbulence. However, the α_{GSF} values ranged between a Gaussian-K41 value of 0.395±0.002 during the end of solar minimum, 1997, to the IK value of 0.246±0.005 during the recurrent fast streams of 2003. This peak in complexity was also apparent in the scaling exponents for v_{sw}, and to a lesser extent B^2.

Finally, we experimented with conditioning the data in a variety of ways (Kiyani et al., 2006) and fitting the data over slightly different ranges of temporal scale. The scaling exponents typically changed by ∼0.01, but overall similar results were still obtained.

5 Discussion and summary

In this study we aimed to show the solar cycle changes in the scaling exponents for small-scale (<2–4 h) inertial range turbulence in the solar wind. The analysis concentrated on a small set of solar wind parameters, namely v_{sw}, B^2, $\sin^4(\theta/2)$, and ε, with a view toward comparison with the results of similar long-term studies of ionospheric and magnetospheric activity. There is no doubt the PDFs of fluctuating solar wind parameters evolved between different temporal scales and fluctuation size (Figs. 3–5). Hence there is reason to believe the observed solar cycle changes in the estimated ε scaling exponents were genuine. The theoretical explanation for these changes is unknown to us, but they may be related to anisotropies in the turbulence (Chapman and Hnat, 2007[1]), and the development of intermittency, as in the two component model of Alfvénic turbulence (Ruzmaikin et al., 1995).

However, some minor issues may have affected the accuracy of our estimated scaling exponents:

1. The time series of solar wind parameters include fluctuations due to inertial range turbulence, but also fluctuations due to other physical processes (e.g. shock fronts). Although impractical for the long-term data sets analysed here, fluctuations due to non-inertial structures could in principle be filtered from the time series (e.g. Borovsky and Funsten, 2003). This might reduce some of the variability in the scaling exponents.

2. It is remarkable that the 6-th order statistical moments estimated using concurrent Wind and ACE measurements during 1998 agreed so well (not shown). However, the slight mismatch between the corresponding solar wind scaling exponents illustrates the difficulty of comparing the results obtained with different spacecraft. Ideally, spacecraft detectors need to be designed and calibrated to guarantee calculation of the same higher order statistical moments when measuring the same physical process. The detector performance also needs to be very stable for a long-term study of this kind, which is believed to be the case for both Wind and ACE.

3. The GSF analysis used here was approximate in the sense that it aimed to identify mono-fractal scaling regimes for solar wind parameters which exhibit multi-fractal behaviour (e.g., v_{sw}). However, analysing the fluctuations on temporal scales of ∼1 min to 2 h helped ensure the fluctuations were reasonably mono-fractal. Future calculations of multi-fractal spectra would permit us to more fully characterise the evolution of fluctuations over a broader range of temporal scale. The

larger error bars for the scaling exponents estimated using Wind data (Fig. 11) suggest stronger multi-fractal behaviour during solar minimum, but so far the ACE spacecraft data has not validated this conclusion.

With these issues in mind, the main results of this study are summarised as follows:

1. Consistent with the properties of Eq. (1), large-scale (∼1 day to years) variations in ε most resembled the large-scale variation in B^2, then v_{sw} (Fig. 2), and least of all $\sin^4(\theta/2)$. Episodes of unusually large ε tended to occur when there were peaks in B^2, but peaks in v_{sw} and $\sin^4(\theta/2)$ also played an important role.

2. The probability density of large fluctuations in v_{sw} minimised at small to medium scales (∼1 min to 1 day) during 1997, the end of solar minimum, and then maximised during the recurrent fast streams of 2003 (Fig. 3). The increase of probability density for large fluctuations in v_{sw} at large scales tended to be compensated by a decrease in probability density of small fluctuations at small scales.

3. Solar cycle changes in the probability density of small fluctuations in B^2 were modest at short τ. However, the probability density of large fluctuations in B^2 at small- to large-scales (∼1 min to 27 day) had a strong minimum during 1996 (Fig. 4). The probability density of large fluctuation in B^2 was decaying during 2005, implying the next solar minimum during 2006–2007. The observed behaviour in B^2 is a familiar signature of solar minimum.

4. Solar cycle changes in small-scale fluctuations of ε were reminiscent of the solar cycle changes in δv_{sw} (Fig. 5). The probability density of large $\delta\varepsilon$ minimised at small scales (∼1 min to 2 h) during 1997, and then maximised during 2003. However, the solar cycle changes in $\delta\varepsilon$ were modest at large τ (∼1 day), and even showed a minimum at the largest scales (∼6.1 day) during the fast streams of 2003 (Fig. 5c).

5. Solar cycle changes in the fluctuations of $\sin^4(\theta/2)$ were the weakest of all. The strong leptokurtic behaviour of $\delta\varepsilon$ arises from the different solar wind parameters in the following order: $\delta\sin^4(\theta/2)$, $\delta(B^2)$, and δv_{sw}, the latter exhibiting the strongest multi-fractal behaviour.

6. The scaling exponents for fluctuations in v_{sw} at small temporal scales (∼1 min to 2 h) were characteristic of intermittent IK turbulence, namely α_{GSF}=0.284±0.001 for the entire data set. However, there was clear evidence that fluctuations in v_{sw} were more complex (α_{GSF}=0.234±0.006) during the recurrent fast streams of 2003 (Fig. 11b).

7. The scaling exponents for fluctuations in B^2 at small temporal scales (∼1 min to 4 h) were between the values expected for Gaussian fluctuations and K41 turbulence, namely α_{GSF}=0.395±0.001. There was also a suggestion that fluctuations in B^2 were more complex during the recurrent fast streams of 2003 (Fig. 11c).

8. The scaling exponents for fluctuations in ε at small scales (∼1 min to 2 h) were the most K41-like, namely α_{GSF}=0.334±0.001. However, α_{GSF} had a Gaussian-K41 value of 0.373±0.005 during the end of solar minimum, 1997, and then decreased to an IK value of 0.247±0.004 during the recurrent fast streams of 2003. The latter was a striking feature (Fig. 11d).

9. Variations in ε at large temporal scales of ∼1 day and greater had a closer resemblance to corresponding variations in B^2 than v_{sw} (Fig. 2). However, variations in $\delta\varepsilon$ at small temporal scales (∼1 min to 2 h) had a closer resemblance to corresponding variations in δv_{sw} than $\delta(B^2)$ (Figs. 3 to 5). Although there were significant solar cycle changes, the scaling exponents were, on average, Gaussian to K41-like for $\delta(B^2)$, K41 to IK-like for $\delta\varepsilon$, and the most IK-like for δv_{sw}.

10. The coupling of solar wind energy to the magnetosphere, as measured by the solar wind ε parameter, had a minimum in complexity (fractal dimension) at the end of solar minimum, 1997, and a maximum in complexity during the recurrent fast streams of 2003. It is important to test whether these results are reproducible from one solar cycle to the next using independent data sets, and to search for corresponding signatures in the magnetosphere.

Acknowledgements. This work was supported by the Australian Research Council, the Australian Antarctic Science Advisory Council, the Australian Academy of Sciences, and the TIGER Consortium Partners (La Trobe University, Australian Antarctic Division, DSTO Intelligence Surveillance and Reconnaissance Division, IPS Radio and Space Services, Monash University, University of Newcastle). K. W. Ogilvie of NASA Goddard Space Flight Center (GSFC) is thanked for allowing us to use Wind solar wind speed data, and R. Lepping of GSFC is thanked for allowing us to use Wind IMF data. D. J. McComas of the Los Alamos National Laboratory is thanked for allowing us to use ACE solar wind speed data, and F. Ness of the Bartol Research Institute is thanked for allowing us to use ACE IMF data. The curators of the NOAA NGDC FTP site are thanked for providing access to sunspot numbers. S. Chapman (Warwick University) and N. Watkins (British Antarctic Survey) are thanked for insightful discussions during their visit supported by the Australian Complex Open Systems Network (COSNET).

Topical Editor I. A. Daglis thanks T. Chang and another referee for their help in evaluating this paper.

References

Benzi, R., Ciliberto, S., Tripiccione, R., et al.: Extended self-similarity in turbulent flows, Phys. Rev. E., 48, R29–R32, 1993.

Bershadskii, A. and Sreenivasan, K. R.: Intermittency and the passive nature of the magnitude of the magnetic field, Phys. Rev. Lett., 93(6), 064501-1 to 4, 2004.

Borovosky, J. E. and Funsten, H. O.: Role of solar wind turbulence in the coupling of the solar wind to the Earth's magnetosphere, J. Geophys. Res., 108(A6), doi:10.1029/2002JA009601, 2003.

Burlaga, L. F.: Interplanetary magnetohydrodynamics, Oxford Univ. Press, New York, 1995.

Burlaga, L. F. and Forman, M. A.: Large-scale speed fluctuations at 1 AU on scales from 1 hour to ≈1 year: 1999 and 1995, J. Geophys. Res., 107(A11), 1403, doi:10.1029/2002JA009271, 2002.

Burlaga, L. F. and F.-Viñas, A.: Multi-scale probability distributions of solar wind speed fluctuations at 1 AU described by a generalised Tsallis distribution, Geophys. Res. Lett., 31, L16807, doi:10.1029/2004GL020715, 2004a.

Burlaga, L. F. and F.-Viñas, A.: Multiscale structure of the magnetic field and speed at 1 AU during the declining phase of solar cycle 23 described by a generalized Tsallis probability distribution function, J. Geophys. Res., 109, A12107, doi:10.1029/2004JA010763, 2004b.

Carroll, B. W. and Ostlie, D. A.: An introduction to modern astrophysics, Addison-Wesley, Reading, Mass, 1996.

Chapman, S. C., Hnat, B., Rowlands, G., and Watkins, N. W.: Scaling collapse and structure functions: identifying self-affinity in finite length time series, Nonlin. Processes Geophys., 12, 767–774, 2005, http://www.nonlin-processes-geophys.net/12/767/2005/.

Crosby, N. B., Meredith, N. P., Coates, A. J., and Iles, R. H. A.: Modelling the outer radiation belt as a complex system in a self-organised critical state, Nonlin. Processes Geophys., 12, 993–1001, 2005, http://www.nonlin-processes-geophys.net/12/993/2005/.

Freeman, M. P., Watkins, N. W., and Riley, D. J.: Evidence for a solar wind origin of the power law burst lifetime distribution of the AE indices, Geophys. Res. Lett., 27(8), 1087–1090, 2000.

Hnat, B., Chapman, S. C., Rowlands, G., Watkins, N. W., and Farrell, W. M.: Finite size scaling in the solar wind magnetic field energy density as seen by WIND, Geophys. Res. Lett., 29(10), 1446, doi:10.1029/2001GL014587, 2002a.

Hnat, B., Chapman, S. C., Rowlands, G., Watkins, N. W., and Freeman, M. P.: Scaling of the solar wind ε and the AU, AL and AE indices as seen by WIND, Geophys. Res. Lett., 29(22), 2078, doi:10.1029/2002GL016054, 2002b.

Hnat, B., Chapman, S. C., Rowlands, G., Watkins, N. W., and Freeman, M. P.: Scaling in long term data sets of geomagnetic indices and solar wind ε as seen by WIND spacecraft, Geophys. Res. Lett., 30(22), 2174, doi:10.1029/2003GL018209, 2003.

Hnat, B., Chapman, S. C., and Rowlands, G.: Scaling and a Fokker-Plank model for fluctuations in geomagnetic indices and comparison with solar wind ε as seen by WIND and ACE, J. Geophys. Res., 110, A08206, doi:10.1029/2004JA010824, 2005.

Horbury, T. S., Balogh, A., Forsyth, R. J., and Smith, E. J.: Magnetic field signatures of unevolved turbulence in solar polar flows, J. Geophys. Res., 101(A1), 405–413, 1996.

Iroshnikov, P. S.: Turbulence of a conducting fluid in a strong magnetic field, Soviet Astronomy, 7, 742–750, 1964.

Kiyani, K., Chapman, S. C., and Hnat, B.: A method for extracting the scaling exponents of a self-affine, non-Gaussian process from a finite length time series, Phys. Rev. E74, 051122, doi:10.1103/PhysRevE.74.051122, 2006.

Kolmogorov, A.: The local structure of turbulence in incompressible viscous fluid for very large Reynolds number, Comp. Rend. Acad. Sci., U.R.S.S., 30, 301–305, 1941.

Kolmogorov, A. N.: A refinement of previous hypothesis concerning the local structure of turbulence in viscous incompressible fluid at high Reynolds number, J. Fluid Mech., 13, 82–85, 1962.

Kraichnan, R. H.: Inertial range spectrum of hydromagnetic turbulence, Phys. Fluids, 8, 1385–1387, 1965.

Lepping, R. P., Acuna, M., Burlaga, L., Farrell, W., Slavin, J., Schatten, K., Mariani, F., Ness, N., Neubauer, F., Whang, Y. C., Byrnes, J., Kennon, R., Panetta, P., Scheifele, J., and Worley, E.: The WIND Magnetic Field Investigation, Space Sci. Rev., 71, 207–229, 1995.

Mandelbrot, B. B.: Gaussian self-affinity and fractals: Globality, the Earth, 1/f noise and R/S, Springer-Verlag, Berlin, 2002.

McComas, D. J., Bame, S. J., Barker, P., Feldman, W. C., Phillips, J. L., Riley, P., and Griffee, J. W.: Solar wind electron proton alpha monitor (SWEPAM) for the Advanced Composition Explorer, Space Sci. Rev., 86, 563–612, 1998.

Ogilvie, K. W., Chorney, D. J., Fitzenreiter, R. J., Hunsaker, F., Keller, J., Lobell, J., Miller, G., Scudder, J. D., Sittler Jr., E. C., Torbert, R. B., Bodet, D., Needell, G., Lazarus, A. J., Steinberg, J. T., Tappan, J. H., Mavretic, A., and Gergin, E.: SWE, a comprehensive plasma instrument for the WIND spacecraft, Space Sci. Rev., 71, 55–77, 1995.

Neugebauer, M. and Snyder, C. W.: Mariner 2 observations of the solar wind 2: Average properties, J. Geophys. Res., 71, 4469, 1963.

Parkinson, M. L.: Dynamical critical scaling of electric field fluctuations in the greater cusp and magnetotail implied by HF radar observations of F-region Doppler velocity, Ann. Geophys., 24, 689–705, 2006, http://www.ann-geophys.net/24/689/2006/.

Perreault, P. and Akasofu, S.-I.: A study of geomagnetic storms, Geophys. J. Roy. Astron. Soc., 54, 547–573, 1978.

Reid, G. C.: Solar variability and its implications for the human environment, J. Atmos. Solar-Terr. Phys., 61, 3–14, 1999.

Ruzmaikin, A., Feynman, J., Goldstein, E. J., Smith, E. J., and Balogh, A.: Intermittent turbulence in solar wind from the south polar hole, J. Geophys. Res., 100(A1), 3395–3403, 1995.

Rycroft, M. J.: The Global atmospheric electric circuit, solar activity and climate change, J. Atmos. Solar-Terr. Phys., 62, 1563–1576, 2000.

Sarabhai, V.: Some consequences of non-uniformity of solar wind velocity, J. Geophys. Res., 68, 1555, 1963.

Smith, C. W., Acuna, M. H., Burlaga, L. F., L'Heureux, J., Ness, N. F., and J. Scheifele, J.: The ACE Magnetic Field Experiment, Space Sci. Rev., 86, 613–632, 1998.

Sornette, D.: Critical phenomena in natural sciences; chaos, fractals, selforganization, and disorder; concepts and tools, Springer-Verlag, Berlin, 2000.

Svensmark, H. and Friis-Christensen, E.: Variations of cosmic ray flux and global cloud coverage-a missing link in solar-climate relationships, J. Atmos. Solar-Terr. Phys., 59, 1225–1232, 1997.

Tijms, H.: Understanding probability: chance rules in everyday life,

Cambridge University Press, Cambridge, 2004.

Tsallis, C.: Possible Generalization of Boltzmann-Gibbs statistics, J. Stat. Phys., 52, 479–487, 1988.

Uritsky, V. M., Klimas, A. J., and Vassiliadis, D.: Comparative study of dynamical critical scaling in the auroral electrojet index versus solar wind fluctuations, Geophys. Res. Lett., 28(19), 3809–3812, 2001.

Yordanova, E., Bergman, J., Consolini, G., Kretzschmar, M., Materassi, M., Popielawska, B., Roca-Sogorb, M., Stasiewicz, K., and Wernik, A. W.: Anisotropic scaling features and complexity in magnetospheric-cusp: a case study, Nonlin. Processes Geophys., 12, 817–825, 2005, http://www.nonlin-processes-geophys.net/12/817/2005/.